Monthly Notices of the ROYAL ASTRONOMICAL SOCIETY

MNRAS **476,** 2339–2351 (2018) doi:10.1093/mnras/sty273
Advance Access publication 2018 February 1

The SAMI Galaxy Survey: gas content and interaction as the drivers of kinematic asymmetry

J. V. Bloom,[1,2]★ S. M. Croom,[1,2] J. J. Bryant,[1,2,3] A. L. Schaefer,[1,2,3] J. Bland-Hawthorn,[1] S. Brough,[2,4] J. Callingham,[1,2,5] L. Cortese,[6] C. Federrath,[7] N. Scott,[1,2] J. van de Sande,[1] F. D'Eugenio,[7] S. Sweet,[8] C. Tonini,[8] J. T. Allen,[1] M. Goodwin,[3] A. W. Green,[3] I. S. Konstantopoulos,[2,9] J. Lawrence,[3] N. Lorente,[3] A. M. Medling,[7,10] M. S. Owers,[3,11] S. N. Richards[1,2,3] and R. Sharp[7]

[1]*Sydney Institute for Astronomy, School of Physics, University of Sydney, NSW 2006, Australia*
[2]*CAASTRO: ARC Centre of Excellence for All-sky Astrophysics*
[3]*Australian Astronomical Observatory (AAO), 105 Delhi Rd, North Ryde, NSW 2113, Australia*
[4]*School of Physics, University of New South Wales, NSW 2052, Australia*
[5]*CSIRO Astronomy & Space Science P.O.Box 76, Epping, NSW 1710, Australia*
[6]*International Centre for Radio Astronomy Research, University of Western Australia, 35 Stirling Highway, Crawley, WA, 6009, Australia*
[7]*Research School of Astronomy and Astrophysics, Australian National University, Canberra, ACT 2611, Australia*
[8]*Centre for Astrophysics and Supercomputing, Swinburne University of Technology, PO Box 218, Hawthorn, VIC 3122, Australia*
[9]*Atlassian 341 George St Sydney, NSW 2000, USA*
[10]*Cahill Center for Astronomy and Astrophysics, California Institute of Technology, MS 249-17 Pasadena, CA 91125, USA*
[11]*Department of Physics and Astronomy, Macquarie University, NSW 2109, Australia*

Accepted 2018 January 12. Received 2018 January 12; in original form 2017 July 9

ABSTRACT

In order to determine the causes of kinematic asymmetry in the Hα gas in the SAMI (Sydney–AAO Multi-object IFS) Galaxy Survey sample, we investigate the comparative influences of environment and intrinsic properties of galaxies on perturbation. We use spatially resolved Hα velocity fields from the SAMI Galaxy Survey to quantify kinematic asymmetry ($\overline{v_{\rm asym}}$) in nearby galaxies and environmental and stellar mass data from the Galaxy And Mass Assembly survey. We find that local environment, measured as distance to nearest neighbour, is inversely correlated with kinematic asymmetry for galaxies with $\log(M_*/{\rm M}_\odot) > 10.0$, but there is no significant correlation for galaxies with $\log(M_*/{\rm M}_\odot) < 10.0$. Moreover, low-mass galaxies [$\log(M_*/{\rm M}_\odot) < 9.0$] have greater kinematic asymmetry at all separations, suggesting a different physical source of asymmetry is important in low-mass galaxies. We propose that secular effects derived from gas fraction and gas mass may be the primary causes of asymmetry in low-mass galaxies. High gas fraction is linked to high $\frac{\sigma_{\rm m}}{V}$ (where $\sigma_{\rm m}$ is Hα velocity dispersion and V the rotation velocity), which is strongly correlated with $\overline{v_{\rm asym}}$, and galaxies with $\log(M_*/{\rm M}_\odot) < 9.0$ have offset $\overline{\frac{\sigma_{\rm m}}{V}}$ from the rest of the sample. Further, asymmetry as a fraction of dispersion decreases for galaxies with $\log(M_*/{\rm M}_\odot) < 9.0$. Gas mass and asymmetry are also inversely correlated in our sample. We propose that low gas masses in dwarf galaxies may lead to asymmetric distribution of gas clouds, leading to increased relative turbulence.

Key words: techniques: imaging spectroscopy – galaxies: evolution – galaxies: interactions – galaxies: kinematics and dynamics – galaxies: structure.

1 INTRODUCTION

Dwarf galaxies are known to be largely irregular systems (e.g. van Zee, Skillman & Salzer 1998; Cannon et al. 2004; Lelli, Verheijen & Fraternali 2014) with low luminosity. They also typically have higher gas fractions than their larger counterparts (Geha et al. 2006;

★ E-mail: jessicavbloom@gmail.com

Huang et al. 2012), and contain comparatively large disturbances, both as a result of interactions and of stochastic processes (Escala & Larson 2008). Complex Hα kinematics in low stellar mass galaxies are linked to the presence of multiple star-forming clumps (Amorín et al. 2012). Further, dwarfs have been found to have higher turbulent support, compared to rotational support (Barton et al. 2001; Garrido et al. 2005), as well as irregular morphologies (Roberts & Haynes 1994; Mahajan et al. 2015).

One of the primary sources of kinematic disturbance is interaction between galaxies. The formation of dark matter haloes through a series of mergers is also well-established in ΛCDM cosmology, both from theory and observation (Peebles 1982; Cole et al. 2008; Neistein & Dekel 2008). *N*-body simulations suggest that the rate of galaxy and halo mergers should be dependent on redshift, but there are differences in merger rate between the predictions of theory and the results of observation. Indeed, simulated major merger rates are highly variable (Hopkins et al. 2010). As a result, innovative methods of studying the merger rate and influence on galaxy evolution are an important part of understanding the formation of the modern universe. In particular, observations of kinematics are needed to probe beyond morphology.

Integral field spectroscopy (IFS) surveys such as SINS (Shapiro et al. 2008) and ATLAS^{3D} (Cappellari et al. 2011) have used the 2D kinematics of galaxies to find and quantify disturbances in galaxies at high and low redshift. They are, however, limited in scope by their use of monolithic instruments, which requires taking IFS measurements for one object at a time, thus increasing the time necessary to accrue large sample sizes. The Sydney–AAO Multi-object IFS (SAMI) is a multiplexed spectrograph that allows for sample sizes of thousands of galaxies on a much shorter time-scale than is possible with other instruments (Croom et al. 2012). The SAMI Galaxy Survey sample will contain 3600 galaxies selected from a combination of the Galaxy And Mass Assembly (GAMA) survey sample (Driver et al. 2011) and from eight galaxy clusters (Bryant et al. 2015; Owers et al. 2017). The chosen GAMA galaxies reflect a broad range in stellar mass and environment, in accordance with the science drivers of the SAMI Galaxy Survey (Bryant et al. 2015).

Previous large-scale surveys have used images to study disturbance and merger rates (e.g. Conselice, Chapman & Windhorst 2003; Casteels et al. 2013). This work has included techniques such as the counting of close pairs and the Concentration, Asymmetry, Smoothness (CAS) classification scheme (Conselice et al. 2003). Image-based analysis has been used to determine merger rates in the nearby and high-redshift universe (Lotz et al. 2011). However, there are inherent difficulties arising from the influence of Hubble type, and these studies are restricted in the range of perturbations to which they are sensitive (Conselice et al. 2003). For example, at high redshift, galaxies may appear photometrically perturbed, but remain kinematically regular, due to features such as clumped star formation (Shapiro et al. 2008). Kinematics provide a different perspective on galaxies' internal processes, and can be used to probe these processes without bias due to Hubble type or morphological features.

In previous work (Bloom et al. 2017b), we developed a quantitative measure of asymmetry in gas dynamics, $\overline{v_{\rm asym}}$, based on kinemetry and following the method of Shapiro et al. (2008). We found a strong inverse correlation between stellar mass and $\overline{v_{\rm asym}}$. Here, we investigate this relationship further, determining how environment is related to asymmetry.

In Section 2, we briefly review the SAMI instrument and the SAMI Galaxy Survey data used in this work. In Section 3 we describe the GAMA Survey data used here and introduce the kinemetry algorithm as a means of measuring kinematic asymmetry. In Section 4, we show the relationships between environment, asymmetry and stellar mass in our sample. Section 5 contains a discussion of environmental factors and other causes of kinematic asymmetry. We conclude in Section 6. We assume a standard cosmology, with $\Omega_{\rm m} = 0.3, \Omega_{\lambda} = 0.7$, and $\rm H_0 = 70\,km\,s^{-1}\,Mpc^{-1}$.

2 THE SAMI GALAXY SURVEY INSTRUMENT AND SAMPLE

The SAMI instrument is a multiplexed integral field unit on the Anglo–Australian Telescope, which uses imaging fibres, or hexabundles (Bland-Hawthorn et al. 2011; Bryant et al. 2014), to simultaneously produce integral field spectra for multiple objects (Bryant et al. 2011). Each SAMI hexabundle consists of 61 optical fibres, with a total bundle diameter of 15 arcsec. The instrument is installed with a fibre cable feeding to the double-beamed AAOmega spectrograph (Sharp et al. 2006; Croom et al. 2012).

The 3600 galaxies comprising the SAMI Galaxy Survey sample were chosen from the GAMA survey sample (Driver et al. 2009) and eight galaxy clusters forming an additional part of the sample. The galaxies were selected from within the GAMA sample to represent a broad range in environment density and stellar mass. The complete SAMI Galaxy Survey sample contains four volume-limited subsamples and supplementary, low-redshift dwarf galaxies (Bryant et al. 2015).

The key data products from the SAMI Galaxy Survey data reduction pipeline are data cubes, from which emission line maps are derived. A full description of the SAMI Galaxy Survey data reduction pipeline can be found in Sharp et al. (2015).

The current paper builds on the work of Bloom et al. (2017b), and uses similar data products from the SAMI Galaxy Survey, including LZIFU. LZIFU is a spectral fitting pipeline written in IDL (Interactive Data Language), performing flexible emission line fitting in the SAMI Galaxy Survey data cubes. The LZIFU pipeline products are 2D kinematic and emission line strength maps for user-assigned lines. A more complete description of the LZIFU pipeline can be found in Ho et al. (2016).

In this work, we used SAMI Galaxy Survey internal data release v.0.9.1. This provided 1021 galaxies that had been observed and processed through the LZIFU pipeline. In previous work, we used an Hα signal-to-noise ratio (S/N) cut of 10 to exclude noisy spaxels from the velocity fields output by LZIFU. Here, we relax the S/N cut to 6. The median velocity error did not increase, so we found that this increased the number of galaxies in the sample without compromising data quality. 827 galaxies met the S/N cut requirements and yielded results from kinemetry, a 230 per cent increase on the sample size in Bloom et al. (2017b). Note that we do not use cluster galaxies in this sample.

3 INPUT DATA

3.1 Environment and stellar mass

This work uses data from the GAMA Survey. Environment measurements are taken from the G3CGal Groups catalogue (Robotham et al. 2011), the Environment Measures catalogue (Brough et al. 2013), and distances to the first nearest neighbour. From the Environment Measures catalogue we take the distance to fifth nearest neighbour, d_5. The d_5 calculations are done on a density defining pseudo-volume-limited population of galaxies in the

GAMA sample. The first nearest neighbour distances, d_1, are calculated similarly to Robotham et al. (2014). They are projected distances between GAMA galaxies. The maximum allowed separation is 5 Mpc or the distance to the nearest sample edge, whichever is closest, and the allowable redshift offset between paired galaxies is $\pm 1000\,\mathrm{km\,s^{-1}}$. The mean redshift of the two galaxies is the redshift at which the separation is calculated.

The stellar mass measurements are from the GAMA Survey catalogue StellarMasses (Taylor et al. 2011), and are based on *ugriz* SEDs constructed from matched aperture photometry. Typical errors are 0.1 dex.

3.2 Kinematic asymmetry

Kinemetry is a generalization of photometry to the higher order moments of the line-of-sight velocity distribution (Krajnović et al. 2006). The kinemetry code is written in IDL, and can be found at http://davor.krajnovic.org/idl/. It was used, for example, to map and quantify asymmetries in the stellar velocity (and velocity dispersion) maps of galaxies in the ATLAS^{3D} survey (Krajnović et al. 2011).

The algorithm models kinematic maps as a sequence of concentric ellipses, with parameters defined by the galaxy kinematic position angle (PA), centre and ellipticity. It is possible to fit the latter two parameters within kinemetry, or to determine them by other means and exclude them from the fitting procedure. For each ellipse, the kinematic moment is extracted and decomposed into the Fourier series:

$$K(a,\psi) = A_0(a) + \sum_{n=1}^{N} (A_n(a)\sin(n\psi) + B_n(a)\cos(n\psi)), \quad (1)$$

where ψ is the azimuthal angle in the galaxy plane, and a is the ellipse semi-major axis length. Points along the ellipse perimeter are sampled uniformly in ψ, making them equidistant in circular projection. The series can be expressed more compactly, as (Krajnović et al. 2006):

$$K(a,\psi) = A_0(a) + \sum_{n=1}^{N} k_n(a)\cos[n(\psi - \phi_n(a))], \quad (2)$$

with the amplitude and phase coefficients (k_n, ϕ_n) defined as:

$$k_n = \sqrt{A_n^2 + B_n^2} \quad (3)$$

and

$$\phi_n = \arctan\left(\frac{A_n}{B_n}\right). \quad (4)$$

The moment maps for both velocity and velocity dispersion are thus described by the geometry of the ellipses and power in the coefficients k_n of the Fourier terms as a function of a (Krajnović et al. 2006). The velocity field of a perfect disc, with no asymmetries, would be entirely expressed by the $\cos(\psi)$ term of equation (1), with zero power in the higher order modes, since the velocity peaks at the galaxy major axis and goes to zero along the minor axis. Accordingly, the power in the B_1 term represents circular motion, with deviations carried in the other coefficients. Analogously, a map of the velocity dispersion field of a perfectly regular, rotating disc would have all power in the A_0 term (i.e. radial dispersion gradient) (Krajnović et al. 2006). The velocity dispersion field is an even moment of the LOSVD, and thus its kinematic analysis reduces to traditional surface photometry.

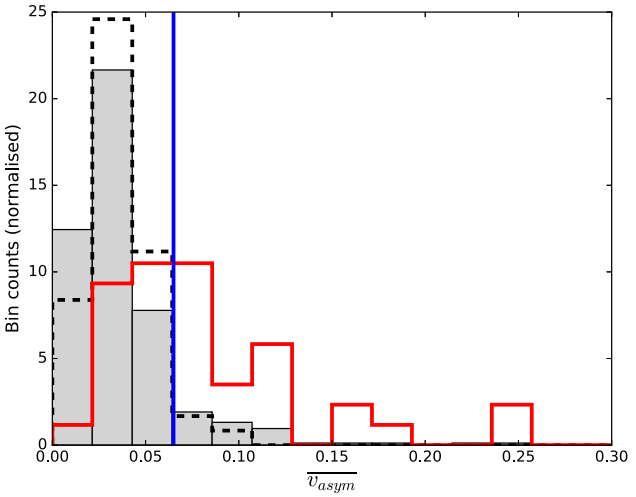

Figure 1. Histogram of $\overline{v_{\mathrm{asym}}}$ for the full sample in this work (grey) and galaxies classified as normal (black, dashed) and perturbed (red) in previous work. The asymmetry cutoff from Bloom et al. (2017b) is shown in blue. Visually classified asymmetric and normal galaxies are seen to have offset distributions of $\overline{v_{\mathrm{asym}}}$, as in Bloom et al. (2017b).

In Bloom et al. (2017b) we defined a quantitative metric, $\overline{v_{\mathrm{asym}}}$, to parametrize kinematic asymmetry in the SAMI Galaxy Survey sample, derived from kinemetry (Krajnović et al. 2006; Shapiro et al. 2008) and this was validated by comparison to a thorough by-eye classification based on Sloan Digital Sky Survey (SDSS) imaging.

The kinemetry algorithm fits a series of regularly spaced, concentric ellipses, from which radial moment values are taken. The ellipses are fitted with parameters defined by the galaxy centre, kinematic PA, and ellipticity. Ellipticities are calculated using 400 arcsec *r*-band cutout images from SDSS. The input image is processed with SEXTRACTOR to mask out neighbouring objects. PSFEx is used to build a model PSF at the location of the galaxy centre. The ellipticity is then found as a light-weighted mean for the whole galaxy, using the Multi-Gaussian Expansion (MGE) technique (Emsellem, Monnet & Bacon 1994) and code from Cappellari (2002). For more detail, we refer to D'Eugenio et al (in preparation). We slightly alter the method in Bloom et al. (2017b) and use the kinematic, rather than photometric PA. We do this because we wish to isolate the effects of misalignment between the photometric and kinematic PA from other forms of atypical kinematics (see Section 5.1). The kinematic PA is calculated by the FIT_KINEMATIC_PA routine from Krajnović et al. (2006). The combination of the fitted ellipses is used to construct individual moment maps. As in Bloom et al. (2017b), and following Shapiro et al. (2008),

$$\overline{v_{\mathrm{asym}}} = \overline{\left(\frac{k_3 + k_5}{2k_1}\right)} \quad (5)$$

where k_1, k_3, k_5 are the coefficients of the Fourier decomposition of the first, third, and fifth order moments of the line-of-sight velocity distribution, respectively. Regular rotation is carried in the k_1 term, and asymmetry in the odd higher order terms. We do not use the even higher order modes because these carry asymmetry in the velocity dispersion.

Fig. 1 shows the distribution of $\overline{v_{\mathrm{asym}}}$ for the full sample in this work (grey), with galaxies visually classified in Bloom et al. (2017b) as normal (black, dashed) and perturbed (red) and the asymmetry cutoff in Bloom et al. (2017b). Note that the sample in Bloom et al.

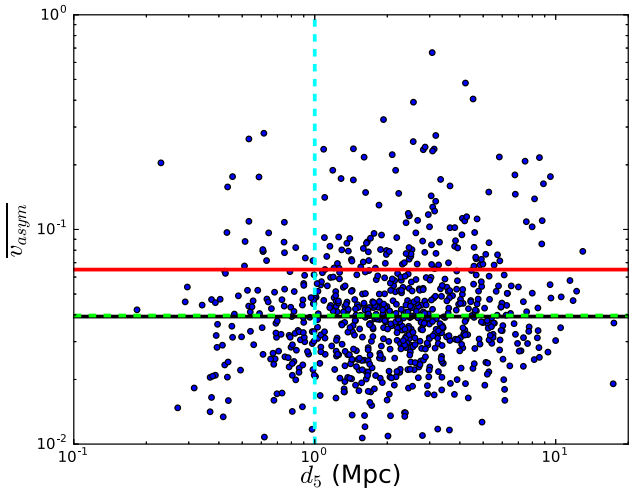

Figure 2. $\overline{v_{\rm asym}}$ against d_5, the comoving distance between a galaxy and its fifth nearest neighbour. The cyan line is at 1Mpc, distinguishing between galaxies close to and far from their fifth nearest neighbour. The red line shows the asymmetry cutoff at $\overline{v_{\rm asym}} = 0.065$, from Bloom et al. (2017b). The black and green lines are the median $\overline{v_{\rm asym}}$ for galaxies in dense and sparse environments, respectively, and there is no significant offset between them. We conclude that there is no correlation between the fifth nearest neighbour distance and the kinematic asymmetry.

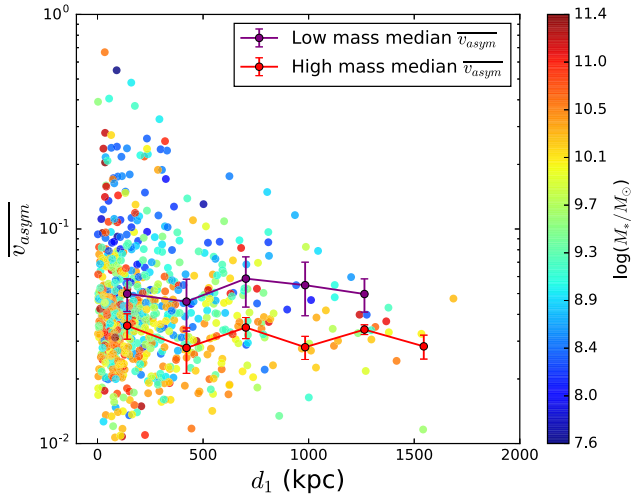

Figure 3. $\overline{v_{\rm asym}}$ against the comoving distance between a galaxy and its first nearest neighbour, d_1, with points coloured by stellar mass. There is an inverse correlation between stellar mass and d_1, as well as stellar mass and $\overline{v_{\rm asym}}$. There is a weak inverse correlation between d_1 and $\overline{v_{\rm asym}}$ for galaxies with $\log(M_*/{\rm M}_\odot) > 10.0$, but not for the rest of the sample. The connected points show median asymmetry for galaxies with $\log(M_*/{\rm M}_\odot) > 10.0$ (red) and $\log(M_*/{\rm M}_\odot) < 9.0$ (purple), in bins of separation. In all cases, low stellar mass galaxies have higher median asymmetry.

(2017b) was smaller than that used in this work, so the galaxies classified as normal and asymmetric in Fig. 1 do not comprise the full sample used here. Visually asymmetric and normal galaxies are seen to have offset distributions of $\overline{v_{\rm asym}}$. We note that we also make use of this metric in Bloom et al. (2017a), in an identical manner to that described above.

4 ASYMMETRY VERSUS STELLAR MASS AND DISTANCE TO NEAREST NEIGHBOUR

4.1 Distance to fifth nearest neighbour and $\overline{v_{\rm asym}}$

Fig. 2 shows the comoving distance to a galaxy's fifth nearest neighbour (in Mpc) (Brough et al. 2013), henceforth d_5, against $\overline{v_{\rm asym}}$. We find no relationship between $\overline{v_{\rm asym}}$ and d_5. A Spearman rank correlation test of $\overline{v_{\rm asym}}$ and d_5 gives $\rho = 0.039, p = 0.28$. We define a cutoff distance of 1 *Mpc* to delineate galaxies 'far' from and 'near' to their fifth nearest neighbour. The median $\overline{v_{\rm asym}}$ for far galaxies is 0.040 ± 0.0001, and for near galaxies it is 0.039 ± 0.0005. That is, there is no offset in the median of the two distributions. These results do not change for different distance cutoffs, or for different ranges of stellar mass.

4.2 First nearest neighbour, stellar mass, and $\overline{v_{\rm asym}}$

Close pairs are frequently used as a proxy indicator of mergers (e.g. Darg et al. 2010; Ellison et al. 2013; Robotham et al. 2014; Barrera-Ballesteros et al. 2015). Accordingly, we measure the distance to the first nearest neighbour, with close distances being assumed to entail interaction.

Fig. 3 shows distance to nearest neighbour against asymmetry. We colour the points by stellar mass, and see that there is an inverse correlation between stellar mass and asymmetry, confirming the results of Bloom et al. (2017b), with a Spearman rank correlation test giving $\rho = -0.23, p = 1 \times 10^{-7}$. There is a weak inverse correlation between $\overline{v_{\rm asym}}$ and d_1 for galaxies with $\log(M_*/{\rm M}_\odot) > 10.0$, with $\rho = -0.19, p = 7 \times 10^{-4}$. For galaxies with $\log(M_*/{\rm M}_\odot) < 10.0$, there is no significant correlation, with $\rho = 0.016, p = 0.74$. For a more detailed exploration of the 'transition' mass at which a correlation is significant, see Appendix A.

Fig. 3 also shows median asymmetry for low and high stellar mass galaxies, in bins of separation. This isolates the effects of environment and stellar mass by splitting the populations. Across the sample, low stellar mass galaxies have higher median asymmetry, regardless of distance to nearest neighbour. The median difference across all stellar mass bins is 0.018 ± 0.003. Fig. 4 shows histograms of $\overline{v_{\rm asym}}$ for different stellar mass populations across two ranges of d_1, chosen to be less than and greater than the median of d_1, respectively. In both bins of d_1, galaxies with $\log(M_*/{\rm M}_\odot) < 9.0$ have a distribution of $\overline{v_{\rm asym}}$ shifted towards higher values. We note that the following results do not change when different values are chosen as a cutoff for d_1.

A two-sample Kolmogorov–Smirnov test of the distributions of asymmetries of galaxies with $\log(M_*/{\rm M}_\odot) < 10.0$ and those with $\log(M_*/{\rm M}_\odot) > 10.0$ gives $p = 4 \times 10^{-5}$. When the sample is divided into bins of d_1, as in Fig. 4, similar results are produced from separate two-sample Kolmogorov–Smirnov tests. When testing the distributions of $\overline{v_{\rm asym}}$ for high-mass galaxies across the d_1 bins in Fig. 4, the same test shows that the distributions are different ($p = 4 \times 10^{-2}$, i.e. marginal significance). However, this is not the case for low-mass galaxies ($p = 6 \times 10^{-1}$). We conclude that there are global differences in the distribution of asymmetries for high- and low-mass galaxies. Fig. 5 shows these patterns more clearly, with d_1 against $\overline{v_{\rm asym}}$ in bins of stellar mass. As the scatter in the relationship in the $\log(M_*/{\rm M}_\odot) > 10.0$ panel is large, we also show the median d_1 for galaxies with $\overline{v_{\rm asym}} > 0.065$ and $\overline{v_{\rm asym}} > 0.065$ for all three subsamples. There is a large offset (71 ± 39kpc) between these medians in the $\log(M_*/{\rm M}_\odot) > 10.0$ sample, but not in the lower mass cases.

There is considerable scatter in the distributions of $\overline{v_{\rm asym}}$ against d_1. Fig. 6 shows the root mean square (rms) of the distribution of $\log(\overline{v_{\rm asym}})$ in bins of d_1, for high- and low-mass galaxies. Errors are

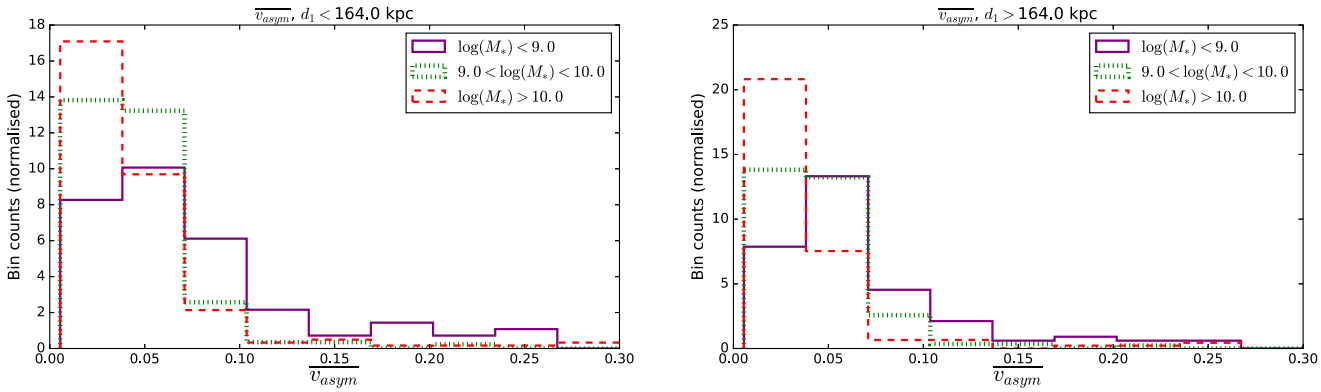

Figure 4. Histograms of $\overline{v_{\rm asym}}$, in bins of stellar mass (dashed, dotted, and solid lines for $\log(M_*/{\rm M}_\odot) > 10.0$, $9.0 < \log(M_*/{\rm M}_\odot) < 10.0$, and $\log(M_*/{\rm M}_\odot) < 9.0$, respectively) across two ranges of d_1. In both d_1 ranges, galaxies with $\log(M_*/{\rm M}_\odot) < 9.0$ have higher distributions of $\overline{v_{\rm asym}}$.

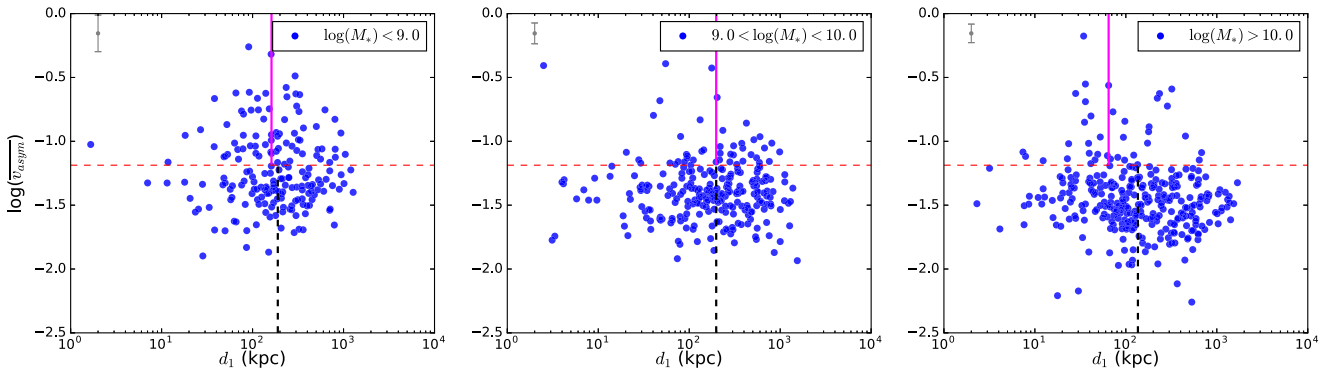

Figure 5. d_1 against $\overline{v_{\rm asym}}$, in bins of stellar mass. There is a weak inverse correlation between d_1 and $\overline{v_{\rm asym}}$ for galaxies with $\log(M_*/{\rm M}_\odot) > 10.0$, but not for the two lower stellar mass bins. Low and high stellar mass galaxies also have different distributions of $\overline{v_{\rm asym}}$ and d_1. Typical error bars are shown in grey (top left corner), and the $\overline{v_{\rm asym}} > 0.065$ cutoff from Bloom et al. (2017b) is shown in red (dashed). The median d_1 for galaxies with $\overline{v_{\rm asym}} > 0.065$ (pink, 65 ± 33kpc) and $\overline{v_{\rm asym}} > 0.065$ (black, dashed, 135 ± 22kpc) is shown for all three subsamples. There is a statistically significant offset of 71 ± 39kpc between these medians in the $\log(M_*/{\rm M}_\odot) > 10.0$ sample, but not in the lower mass cases.

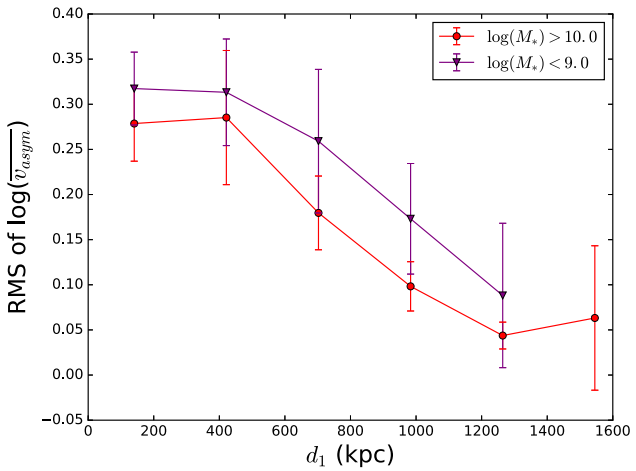

Figure 6. rms of the distribution of $\log(\overline{v_{\rm asym}})$ in bins of d_1, for both high- and low-mass galaxies. At all d_1, there is more scatter in the distribution of galaxies with $\log(M_*/{\rm M}_\odot) < 9.0$ than for those with $\log(M_*/{\rm M}_\odot) > 10.0$. At low d_1, there is an increase in the rms of the distribution of $\overline{v_{\rm asym}}$ for high-mass galaxies, but low-mass galaxies show only a weak change in distribution.

produced by bootstrapping 100 iterations of adding random noise (based on uncertainties in $\overline{v_{\rm asym}}$) to the distribution of $\overline{v_{\rm asym}}$ within each mass bin. At all d_1, the scatter in the distribution of $\overline{v_{\rm asym}}$ of galaxies with $\log(M_*/{\rm M}_\odot) < 9.0$ is larger than for galaxies with $\log(M_*/{\rm M}_\odot) > 10.0$. At low d_1, there is an increase in scatter for high-mass galaxies, but only weak evidence of this effect in the low-mass population. Despite this difference in significance, the overall trends in the two populations look similar. A larger sample may thus result in a significant result for the low-mass galaxies as well.

Fig. 7 shows $\overline{v_{\rm asym}}$ against d_1, with the fractional count of galaxies with $\overline{v_{\rm asym}} > 0.065$ for high- and low-mass populations, respectively. There is no significant decrease in fractional count with increased d_1 for either population of galaxies.

In order to test whether the calculated correlation in the $\log(M_*/{\rm M}_\odot) > 10.0$ case of Fig. 5 is significant, we resampled the $\overline{v_{\rm asym}}$ values within Gaussian distributions centred on the calculated value, with width equal to the error and then recalculated the correlation coefficients, over 1000 iterations. We found that, for all 1000 cases, $-0.25 < \rho < -0.13$ and $p < 0.018$. Further, 60 per cent of p-values were $<3\sigma$. The same test on the $\log(M_*/{\rm M}_\odot) < 9.0$ data gave ranges of $-0.1 < \rho < 0.5$, $0.3 < p < 1.0$. Thus, whilst the trend is of equal size to the scatter, it is still significant.

Fig. 8 replicates Fig. 3, but with colours coded by the ratio of stellar masses of galaxies to those of their nearest

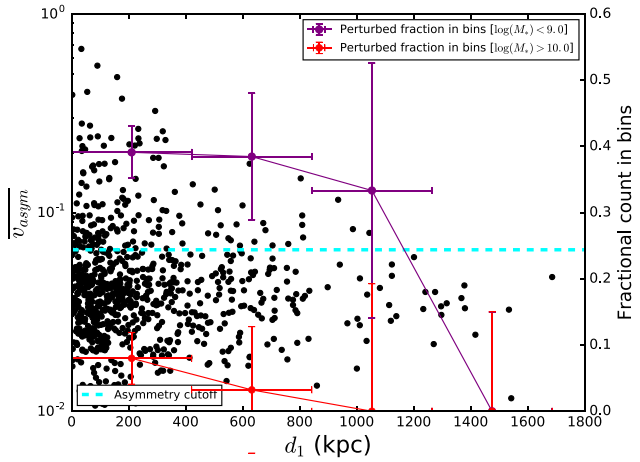

Figure 7. $\overline{v_{\rm asym}}$ against d_1, with the fractional count of galaxies with $\overline{v_{\rm asym}} > 0.065$ for high (red) and low (purple) mass populations. The asymmetry cutoff at $\overline{v_{\rm asym}} = 0.065$ is shown in cyan (dashed). There is no significant decrease in fractional count with increased d_1.

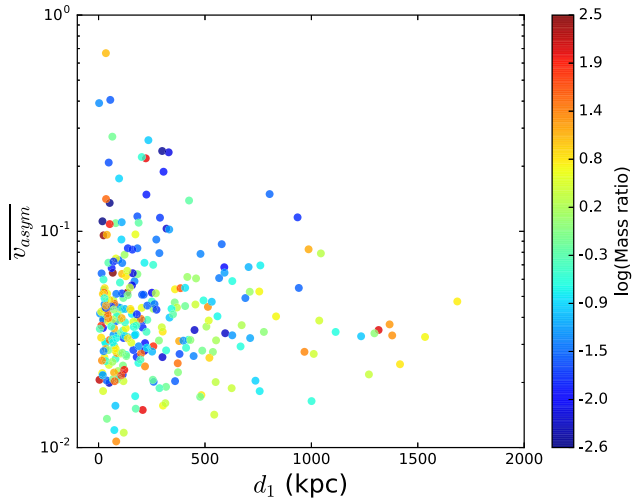

Figure 8. $\overline{v_{\rm asym}}$ against the comoving separation between galaxies and their (first) nearest neighbours, with points coloured by the ratio between the stellar masses of galaxies and their nearest neighbours. There is a relationship between mass ratio and $\overline{v_{\rm asym}}$, but it appears to be dependent on the underlying relationship between mass ratio and stellar mass.

neighbours. A Spearman rank correlation test between mass ratio $(\log(M_*/{\rm M}_\odot)_1 - \log(M_*/{\rm M}_\odot)_2$ and asymmetry yields $\rho = -0.21$, $p = 0.0029$, and the same test between mass ratio and distance gives $\rho = -0.16$, $p = 0.026$. However, there is no correlation when the mass range is split into high- and low-mass samples ($\log(M_*/{\rm M}_\odot) > 10.0$, $\log(M_*/{\rm M}_\odot) < 9.0$). Of course, mass ratio and stellar mass are not independent. Indeed, a partial correlation test of mass ratio and asymmetry, taking stellar mass into account, yields $\rho = -0.016$, $p = 0.78$, implying no independent correlation. Further, there is no restriction on d_1 when calculating the mass ratio, and galaxies with massive nearest neighbours at large d_1 are not likely to be perturbed.

Partial Pearson correlation tests for all galaxies in the sample of d_1, $\overline{v_{\rm asym}}$, and stellar mass (Table 1) show that d_1 and $\overline{v_{\rm asym}}$ are independently correlated, as are $\overline{v_{\rm asym}}$ and stellar mass. There is no significant independent relationship between d_1 and stellar mass.

Table 1. Partial Pearson correlation coefficients for stellar mass, d_1, and $\overline{v_{\rm asym}}$. $\overline{v_{\rm asym}}$ and stellar mass remain correlated, ignoring d_1, and likewise for $\overline{v_{\rm asym}}$ and d_1, ignoring stellar mass. There is no partial correlation between d_1 and stellar mass.

x, y	ρ	p
d_1, $\overline{v_{\rm asym}}$	−0.10	0.0046
d_1, $\log(M_*/{\rm M}_\odot)$	−0.067	0.060
$\overline{v_{\rm asym}}$, $\log(M_*/{\rm M}_\odot)$	−0.18	3×10^{-7}

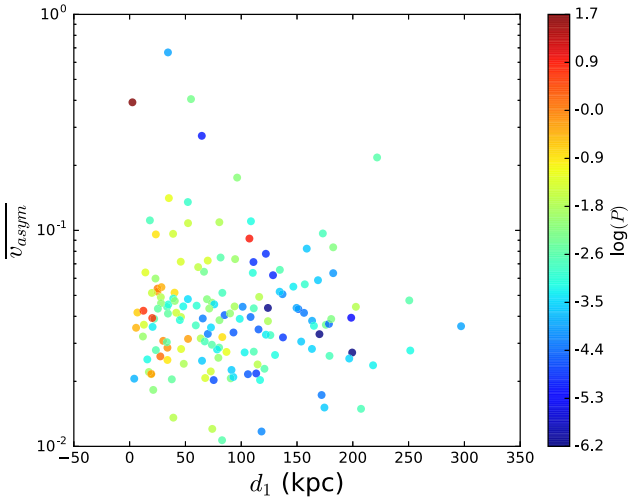

Figure 9. $\overline{v_{\rm asym}}$ against the comoving separation between galaxies and their (first) nearest neighbours, with points coloured by the tidal perturbation parameter P, as described in equation (6). Of course, the strongest relationship is between P (tidal force) and distance, and there is no correlation between P and asymmetry.

d_1 is, of course, only a proxy for interaction. In order to directly measure the gravitational influence exerted on galaxies by their nearest neighbour, Fig. 9 shows d_1 against $\overline{v_{\rm asym}}$ for galaxies in groups (identified using the GAMA Groups catalogue; Robotham et al. 2011) with points coloured by the unitless tidal perturbation parameter from Byrd & Valtonen (1990):

$$P = \frac{M_{\rm rat}}{R^3} \tag{6}$$

where $M_{\rm rat}$ is the mass ratio described above and

$$R = \frac{d_1}{r_{90}} \tag{7}$$

where r_{90} is the radius enclosing 90 per cent of the galaxy's light profile from the Sérsic profile fits in the GAMA catalogue (Kelvin et al. 2012). We only consider galaxies in groups (including pairs) because isolated galaxies, by definition, do not have nearby galaxies. The value for P given here is the maximal value within a galaxy group, i.e. the value of the maximum tidal force exerted by a group member on the subject galaxy, as used in Schaefer et al. (submitted). There is no correlation between P and $\overline{v_{\rm asym}}$ for any mass or d_1 range within the sample. This holds true even when only considering galaxies with $P > 0.1$, which is given by Byrd & Valtonen (1990) as the value above which tidal perturbation is likely to be effective.

In summary we find that, at all nearest neighbour separations, low-mass galaxies have higher asymmetry than high-mass galaxies, suggesting that processes other than interaction influence

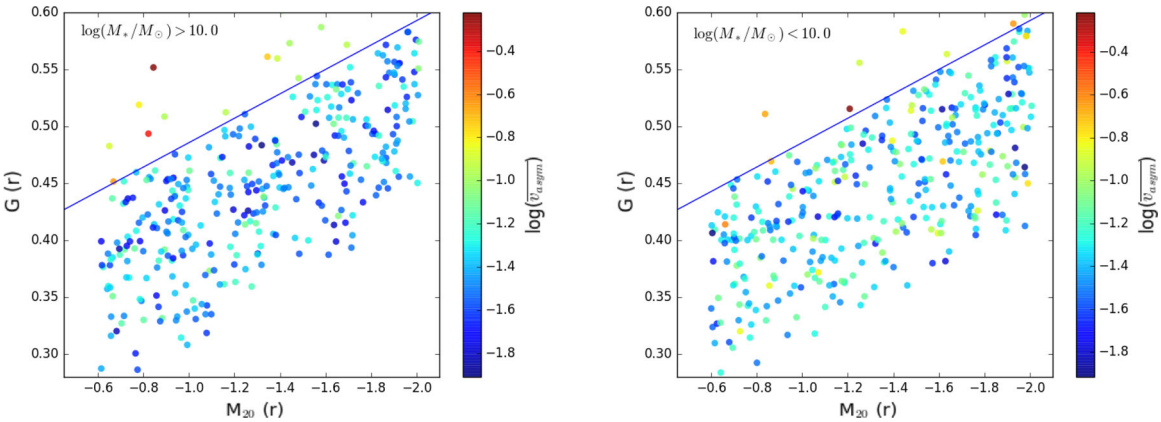

Figure 10. The M_{20}/Gini plane from Lotz et al. (2004), for galaxies with $\log(M_*/M_\odot) > 10.0$ (left) and <10.0 (right), both with points coloured by $\overline{v_{\rm asym}}$. The line delineating galaxies showing features associated with interaction from Lotz et al. (2004) is shown in blue. Whilst all galaxies above the line in both cases are asymmetric, in the high-mass case there are no extremely asymmetric galaxies below the line. In the lower mass case, however, many of the galaxies with the highest value of $\overline{v_{\rm asym}}$ lie below the line. This may indicate that high-mass galaxies with the highest asymmetry are interacting, whereas high asymmetry low-mass galaxies may not necessarily be.

asymmetry for these objects. For high-mass galaxies, asymmetry increases at low d_1, and there is an overall change in the distribution of asymmetries at low d_1, as seen in Fig. 6. Low-mass galaxies show only a weak change in the rms of $\overline{v_{\rm asym}}$ at different d_1, and there is no correlation between d_1 and $\overline{v_{\rm asym}}$. This means that we cannot rule out a change in asymmetry in low-mass galaxies at low d_1, but there is no strong signature of this effect.

5 CAUSES OF KINEMATIC ASYMMETRY

The results in Section 4 are indicative of plural causes of asymmetry in our sample. Further, there is evidence that there may be different primary causes of asymmetry for high- and low-mass galaxies. We here explore three potential causes of asymmetry, and how they affect galaxies with different stellar masses:

(i) interaction between galaxies, either through mergers or tidal disturbance.
(ii) turbulence caused by star formation feedback and other processes linked to high gas fraction.
(iii) asymmetric gas cloud distribution caused by low gas mass.

5.1 Interaction (pre- and post-merger)

Interaction is a known cause of kinematic asymmetry (e.g. Krajnović et al. 2006; Shapiro et al. 2008). Whilst Fig. 3 shows no overall relationship between d_1 and $\overline{v_{\rm asym}}$, Fig. 5 shows that galaxies with $\log M_*/{\rm M}_\odot > 10.0$ show some evidence that asymmetry is correlated with distance to nearest neighbour. The increased rms at low d_1 across both high- and low-mass populations in Fig. 6 also indicates that interaction leads to high asymmetry values. That the dispersion increases at relatively large d_1 also suggests that it may not just be very local, galaxy–galaxy interactions that cause the environmental trends seen in the distribution of $\overline{v_{\rm asym}}$.

In order to test whether asymmetry is caused by interaction, we use quantitative morphology measures Gini, G, and M_{20}, which can be combined to identify merging galaxies as in Lotz, Primack & Madau (2004). The G and M_{20} coefficients are both measures of the distribution of light. G is used to measure inequality in a distribution (Gini 1912), in this case in the spatial distribution of light (Abraham, Van Den Bergh & Nair 2003). High G indicates high concentration of light, and G is defined as (Glasser 1962):

$$G = \frac{1}{\overline{X} n(n-1)} \sum_i^n (2i - n - 1) X_i, \tag{8}$$

where $\overline{X}$ is (in this case) the mean of the galaxy flux in n total pixels, with X_i being the flux in the ith pixel.

The M_{20} coefficient is similar to G, in that it measures the concentration of light within a galaxy, but can be used to distinguish galaxies with different Hubble types (Lotz et al. 2004). The total second-order moment of galaxy flux, $M_{\rm tot}$, is defined as the flux f_i in each pixel, multiplied by the squared distance between pixel i and the centre of the galaxy (x_c, y_c), summed over all galaxy pixels:

$$M_{\rm tot} = \sum_i^n M_i = \sum_i^n f_i[(x_i - x_c)^2 + (y_i - y_c)^2]. \tag{9}$$

M_{20} is then defined as the normalized second-order moment of the brightest 20 per cent of the galaxy's flux. The galaxy pixels are rank-ordered by flux, and then M_i (the second-order moment of light for each pixel i) is summed over the brightest pixels until the sum of the brightest pixels is equal to 20 per cent of the total flux:

$$M_{20} = \log_{10}\left(\frac{\sum_i M_i}{M_{\rm tot}}\right) \tag{10}$$

for $\sum_i f_i < 0.2 f_{\rm tot}$, where $f_{\rm tot}$ is the total flux, $\sum_i^n f_i$.

We use the r-band SDSS DR10 images (Ahn et al. 2014) and follow Lotz et al. (2004) and Conselice, Rajgor & Myers (2008). Fig. 10 shows the M_{20}/Gini plane as in Lotz et al. (2004) for galaxies with $\log(M_*/{\rm M}_\odot) > 10.0$ and <10.0, respectively. The line delineating galaxies showing features associated with interaction suggested by Lotz et al. (2004) is shown in blue. Points are coloured by $\overline{v_{\rm asym}}$.

Whilst all galaxies above the line in both cases are asymmetric, in the high-mass case there are no extremely asymmetric galaxies below the line. In the lower mass case, however, many of the galaxies with the highest value of $\overline{v_{\rm asym}}$ lie below the line. Fig. 11 shows these differences in distribution more clearly. This may indicate that high-mass galaxies with the highest asymmetry are interacting, whereas high asymmetry low-mass galaxies may not necessarily be. Figs 12 and 13 are examples of high-mass galaxies above the line in the high-mass panel in Fig. 10, both with highly disturbed

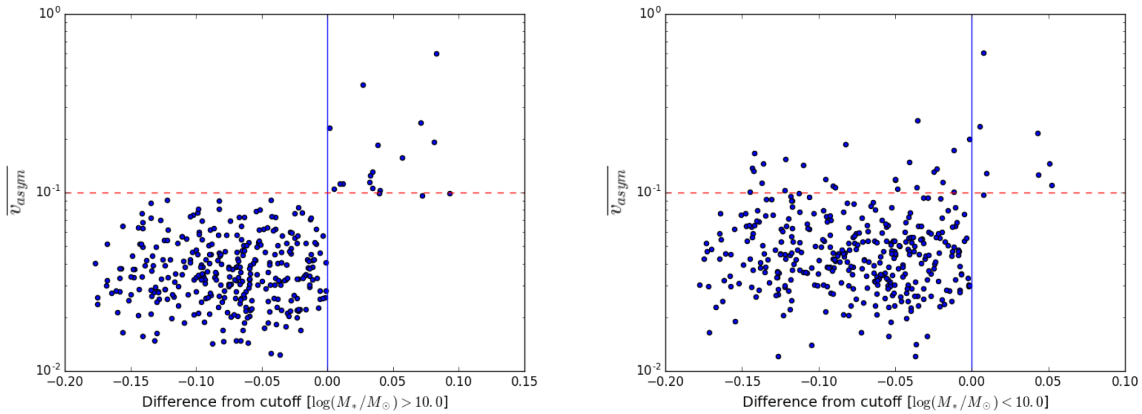

Figure 11. Difference from the line on the M_{20}/Gini plane proposed by Lotz et al. (2004) (zero line shown in blue) against $\overline{v_{\rm asym}}$, for galaxies with $\log(M_*/{\rm M}_\odot) > 10.0$ (left) and <10.0 (right). The red, dashed line shows $\overline{v_{\rm asym}} = 0.1$. In the high-mass case, almost all galaxies with positive difference from the Lotz et al. (2004) line have $\overline{v_{\rm asym}} > 0.1$, and there are none of these very high asymmetry galaxies with negative residuals from the line. In the low-mass case, whilst all galaxies with positive difference from the line have high asymmetry, a significant number of galaxies with $\overline{v_{\rm asym}} > 0.1$ show negative differences, i.e. they appear below the line in Fig. 10.

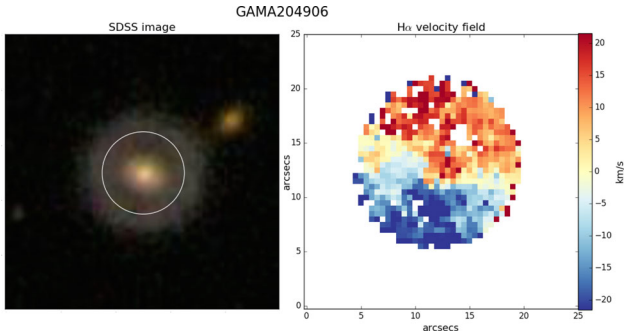

Figure 12. The SDSS image (left) and Hα velocity field (right) for GAMA204906, a galaxy with $\log(M_*/{\rm M}_\odot) = 10.4$ and $\overline{v_{\rm asym}} = 0.11$. It lies above the line from Lotz et al. (2004) in Fig. 10. The SAMI field of view is shown as a white circle.

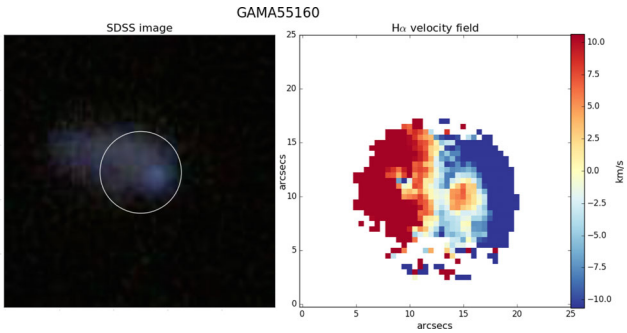

Figure 14. GAMA55160, with $\log(M_*/{\rm M}_\odot) = 8.4$ and $\overline{v_{\rm asym}} = 0.14$. It lies above the line from Lotz et al. (2004) in Fig. 10. The kinematically decoupled core may be the result of an interaction. The SAMI field of view is shown as a white circle.

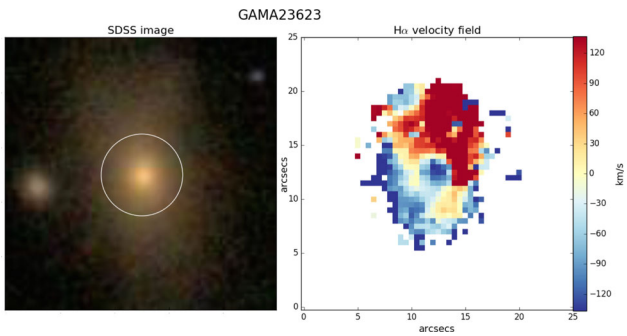

Figure 13. GAMA23623, with $\log(M_*/{\rm M}_\odot) = 11.4$ and $\overline{v_{\rm asym}} = 0.19$. It lies above the line from Lotz et al. (2004) in Fig. 10. The SAMI field of view is shown as a white circle.

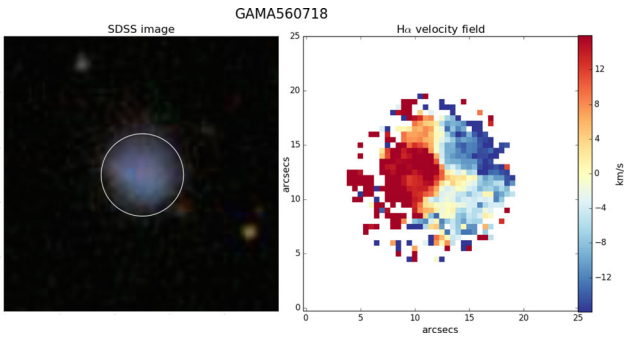

Figure 15. GAMA560718, with $\log(M_*/{\rm M}_\odot) = 7.8$ and $\overline{v_{\rm asym}} = 0.10$. It lies below the line from Lotz et al. (2004) in Fig. 10, indicating that it may not show features of interaction. The SAMI field of view is shown as a white circle.

velocity fields consistent with interaction. Fig. 14 is a low-mass galaxy above the line in the right hand (low-mass) panel of Fig. 10, and shows a kinematically decoupled core, signifying a potential past interaction. By contrast, Fig. 15 shows an asymmetric galaxy *below* the line in the right-hand panel of Fig. 10. We stress that the use of a cutoff mass of $\log(M_*/{\rm M}_\odot) = 10.0$ between the two planes in Figs 10 and 11 contributes to the observed 'cleanness' of the difference between the distributions. Lower mass cuts reduce the distinction between the high- and low-mass samples, so the sharpness of the cutoff at $\log(M_*/{\rm M}_\odot) = 10.0$ should be interpreted with caution.

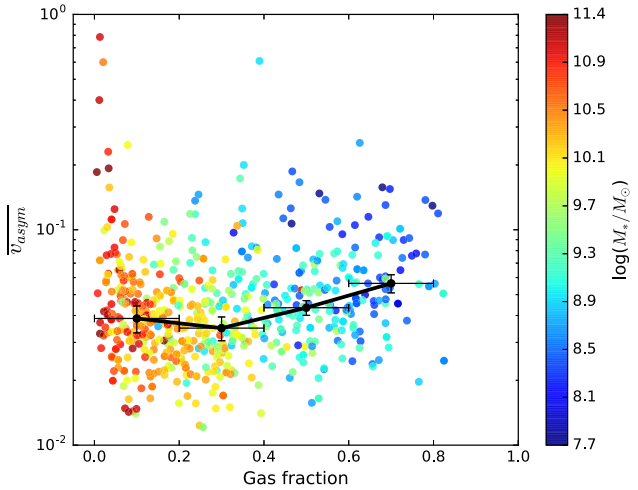

Figure 16. Gas fraction against $\overline{v_{\rm asym}}$ (on a log scale), showing a positive correlation. Points are coloured by $\log(M_*/{\rm M}_\odot)$ This result supports the argument that asymmetry in our sample is linked to increased turbulence resulting from high gas fractions in low stellar mass galaxies. The expected relationship between gas fraction and $\log(M_*/{\rm M}_\odot)$ is also clear, as determined by equation (11). Median asymmetries in bins of gas fraction are shown in black, with horizontal errors indicating bin width and vertical errors indicating the error on the median. There is an upwards trend in the median asymmetry with gas fraction. The first bin has increased $\overline{v_{\rm asym}}$ caused by the interacting outlying galaxies with high $\overline{v_{\rm asym}}$ and $\log(M_*/{\rm M}_\odot)$ and low gas fraction.

The conclusion from the above and Fig. 5 is that stellar mass and distance to nearest neighbour act separately on $\overline{v_{\rm asym}}$, independently producing kinematic asymmetry in galaxies of different mass ranges. In the case of galaxies with $\log(M_*/{\rm M}_\odot) > 10.0$, interaction is a probable cause of asymmetry. However, whilst there will be some asymmetric, low-mass galaxies that are either currently or have recently been interacting, this is not a sufficient explanation for the full range of asymmetry seen in the low-mass sample.

It is also true that there is a large amount of scatter in all cases in Fig. 5. Whilst some galaxies in the $\log(M_*/{\rm M}_\odot)$ can be definitively classified as interacting, and the observed correlation is statistically robust, it is also possible that other factors influence asymmetry in high-mass galaxies, and that this contributes to the scatter in Fig. 5.

In summary, all the statistical tests presented in this work suggest that there is a statistically significant correlation between $\overline{v_{\rm asym}}$ and d_1, at least for galaxies with $\log(M_*/{\rm M}_\odot) > 10.0$. This suggests that galaxy–galaxy interactions are playing a role in driving the degree of asymmetry in at least a fraction of our sample. However, the large scatter present in Figs 3–9 seems to imply that additional factors other than gravitational disturbances alone may also be responsible for the high value of $\overline{v_{\rm asym}}$ observed in our sample.

5.2 Secular processes in low stellar mass galaxies

5.2.1 Dispersion

In our previous work (Bloom et al. 2017b), we postulated that the observed inverse correlation between stellar mass and kinematic asymmetry may be related to the higher gas fraction found in low stellar mass galaxies. Fig. 16 shows a positive correlation ($\rho = 0.14$, $p = 4 \times 10^{-4}$) between estimated gas fraction against $\overline{v_{\rm asym}}$. As we do not have direct gas masses for our sample, atomic gas fractions are estimated from equation (5) in Cortese et al. (2011):

$$\log\left(\frac{M({\rm H\,I})}{M_*/{\rm M}_\odot}\right) = -0.33(NUV - r) - 0.40\log(\mu_*) + 3.37 \tag{11}$$

where $NUV - r$ is the $NUV - r$ magnitude and μ_* is the stellar mass surface density in ${\rm M}_\odot$ kpc^{-2}. We have checked these mass estimates against molecular masses calculated from the star formation rate from non-obscuration affected, sub-mm data as in Federrath et al. (2017) for a sub-sample of our galaxies for which the requisite data were available. We note that we did not use the molecular masses for this work because *Herschel* fluxes were unavailable for the full mass range of our sample. Although there was scatter, the relationship between the mass estimates used here and those calculated from star formation rate was 1:1, implying that the systematic relationships found here would not change if we used the calculated masses. As there is significant scatter in the relationship in Fig. 16, we also show median asymmetries in bins of gas fraction. There is an upwards trend in the median asymmetry with gas fraction. The lowest gas fraction bin has a slightly higher asymmetry than the median trend, driven by the small population of galaxies with high $\overline{v_{\rm asym}}$ and $\log(M_*/{\rm M}_\odot)$ and low gas fraction.

The trend in Fig. 16 is in agreement with literature (Geha et al. 2006; Huang et al. 2012). Work such as Amorín et al. (2012) shows that complex Hα kinematics in low-mass galaxies are linked to the presence of multiple clumps of star formation. We do, however, note that some systems, such as high-redshift sources, are asymmetric in flux but kinematically regular (e.g. Wisnioski et al. (2011)).

For star-forming galaxies, high gas fractions are linked to high $\frac{\sigma_{\rm m}}{V}$, where $\sigma_{\rm m}$ is the mean gas velocity dispersion, and V is the gas circular velocity (Green et al. 2014). The $\sigma_{\rm m}$ values we use are the mean dispersion from the SAMI velocity dispersion maps from LZIFU (not flux-weighted). The V values are taken from arctan fits to the radial k_1 profiles from the fitted kinemetry ellipses extracted as in Section 3.2. The value of the resulting fitted rotation curve is computed at $2.2r_{\rm e}$ (where $r_{\rm e}$ is the effective radius), as this is the point at which the curve is expected to have become flat. For a more thorough explanation of the fitting process, see Bloom et al. (2017a).

Fig. 17 shows $\frac{\sigma_{\rm m}}{V}$ against $\overline{v_{\rm asym}}$ for all galaxies in the sample, with points coloured by stellar mass. Unsurprisingly, there is a strong relationship between $\frac{\sigma_{\rm m}}{V}$ and $\overline{v_{\rm asym}}$, as both measure disturbances away from pure circular rotation. A Spearman rank correlation test of $\frac{\sigma_{\rm m}}{V}$ and $\overline{v_{\rm asym}}$ gives $\rho = 0.56$, $p = 6 \times 10^{-27}$. Median $\frac{\sigma_{\rm m}}{V}$ for galaxies with $\log(M_*/{\rm M}_\odot) < 9.0$, >9.0, and >10.0 are shown as purple, green, and red, respectively. Table 2 gives values for these medians. Low-mass galaxies have significantly higher median $\frac{\sigma_{\rm m}}{V}$ than higher mass galaxies. This is to be expected given V correlates with stellar mass.

In order to isolate the relationship between asymmetry and dispersion, without the dependence on stellar mass, we introduce the T metric, which defines a measure of asymmetry as a fraction of dispersion:

$$T = \overline{\left(\frac{k_3 + k_5}{2 \times k_{0,\sigma}}\right)} \tag{12}$$

where k_3 and k_5, as in Section 3.2, trace kinematic disturbance in the velocity field and $k_{0,\sigma}$ is, analogously to k_1, the radial values of zeroth order moment of the velocity dispersion field. This metric is an adaptation of the $\frac{\sigma_{\rm m}}{V}$ parameter. We use $k_{0,\sigma}$ in this case, rather than $\sigma_{\rm m}$, to increase ease of comparison to $\overline{v_{\rm asym}}$.

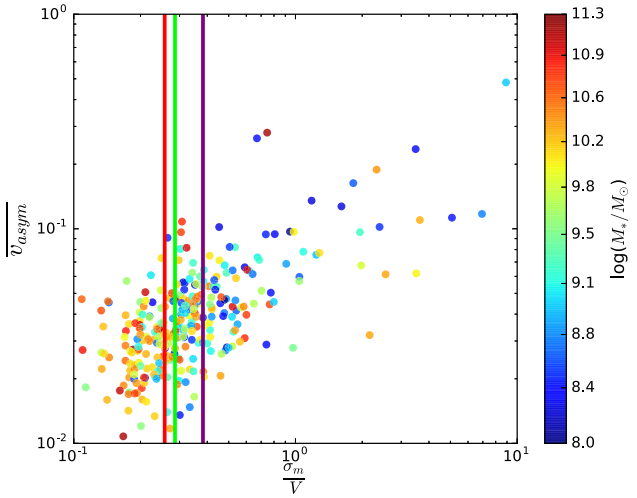

Figure 17. $\frac{\sigma_m}{V}$ against $\overline{v_{asym}}$ (on a log scale), with points coloured by stellar mass. Median $\frac{\sigma_m}{V}$ for galaxies with log (M_*/M$_\odot$) < 9, >9, and >10.0 are shown as purple, green, and red, respectively. There is a significant offset in median $\frac{\sigma_m}{V}$ for galaxies with log (M_*/M$_\odot$) < 9.0.

Table 2. Median $\frac{\sigma_m}{V}$ and median T for galaxies with log (M_*/M$_\odot$) < 9.0, >9.0, and > 10.0, respectively. Low-mass galaxies have both higher median $\frac{\sigma_m}{V}$ on the main sequence and lower median T, indicating that they are both more dispersion-supported overall and have higher dispersion support at a given $\overline{v_{asym}}$ than their higher mass counterparts.

Sample	$\overline{\frac{\sigma_m}{V}}$	$\overline{T}$
log (M_*/M$_\odot$) < 9.0	0.38 ± 0.037	0.036 ± 0.0031
log (M_*/M$_\odot$) > 9.0	0.28 ± 0.019	0.054 ± 0.0033
log (M_*/M$_\odot$) > 10.0	0.25 ± 0.024	0.062 ± 0.0048

Table 2 gives median values for T for different mass ranges. Low stellar mass galaxies have significantly lower $\overline{T}$, i.e. they are more dispersion-supported for given values of $\overline{v_{asym}}$ than higher mass galaxies. There is also a positive Spearman rank correlation between T and stellar mass, with $\rho = 0.38$, $p = 7 \times 10^{-12}$. Fig. 18 shows stellar mass against T, illustrating these relationships. Notably, the galaxies with the highest T are at high stellar mass and, as discussed in Section 5.1, high stellar mass galaxies with high $\overline{v_{asym}}$ show qualitative signs of interaction. This may point to T as a means of distinguishing interacting galaxies from those with asymmetry caused by other processes. In order to confirm that the trend in Fig. 18 is not caused by the outliers with $T > 0.2$, we show fit lines for the full sample and for the sample with those outliers excluded. Whilst the slope decreases slightly, the trend remains with the outliers excluded.

The implication of these results is that low stellar mass galaxies have more small-scale than large-scale asymmetry than high stellar mass galaxies. Further, for given $\overline{v_{asym}}$, low stellar mass galaxies have less fractional rotational support than their high-mass counterparts. This explains the results of Figs 8 and 9, as neither mass ratio nor P would be expected to correlate with asymmetry caused by dispersion.

5.2.2 *Asymmetry of the gas cloud distribution*

Although low stellar mass galaxies have comparatively higher gas *fractions*, they have lower overall gas *masses*, which may affect the

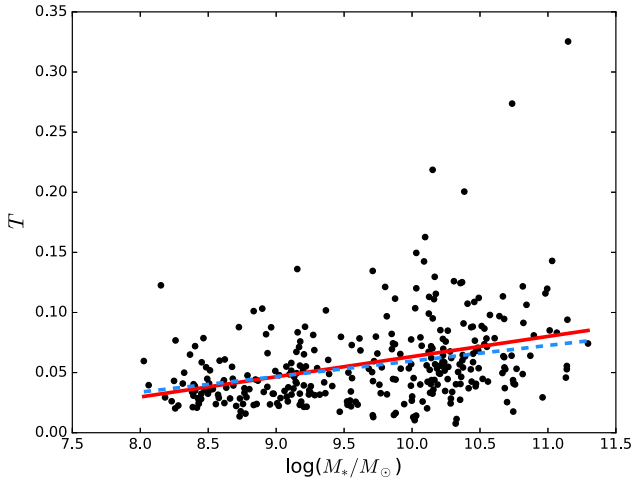

Figure 18. Stellar mass against T (defined in equation 12 as the ratio of the higher order moments of the velocity field to the velocity dispersion). There is a clear relationship, indicating that low stellar mass galaxies have lower velocity perturbation for given dispersions than high-mass galaxies. For clarity, we also show the linear fit to the full sample (red) and the sample excluding the clear outliers with $T > 0.2$ (blue, dashed). The trend remains with the outliers excluded.

distribution of clouds of star-forming gas. Indeed, Fig. 16 shows that at high gas fractions (i.e. >0.4) galaxies with lower stellar mass show larger asymmetry. This seems to suggest that – for dwarf galaxies – it is the gas mass (more than gas fraction relative to other baryonic components) that is linked to the degree of turbulence in the interstellar medium (ISM).

Before discussing the physical implications of this result, it is important to remind the reader that what we plot are not measured cold gas fractions, but are empirical values. Taken at face-value, the x-axis in Fig. 16 should read as a combination of colour and stellar mass surface density, and the residual trends at high gas fractions as a likely secondary role played by either star formation rate and/or galaxy size.

Since all galaxy properties are interconnected, disentangling between cause and effect does require direct cold gas measurements, which are unfortunately unavailable for our sample. However, it is natural to expect that the cold gas content is tightly connected to the degree of kinematic disturbance in the ISM. Thus, in the rest of the paper we assume that Fig. 16 provides a fair representation of the real relation between gas content and $\overline{v_{asym}}$. It will be the key for future works to further test this assumption.

In order to explore the plausibility of gas mass as an influence on $\overline{v_{asym}}$, we create four simple models with different stellar masses [log (M_*/M$_\odot$) = 8.0, 9.0, 10.0, and 11.0, respectively], evenly sampling the stellar mass range of our sample, to investigate the distribution of gas clouds in low- and high-mass galaxies and test this as an explanation for the observed asymmetry–stellar mass relationship.

We divide the disc into six evenly spaced radial bins, after scaling all discs in terms of r_e as in Cecil et al. (2016). The disc is further sub-divided into four azimuthal quadrants, to enable a calculation of spatial asymmetry. We then generate random populations of gas clouds according to several assumptions:

(i) the mass spectrum of clouds is the same across the disc, consistent with the IMF, as in Bland-Hawthorn, Krumholz & Freeman (2010). Given that the mass spectrum of star-forming clouds is 10^3–10^7 M$_\odot$, we take a median value 10^5 M$_\odot$ weighted by IMF slope

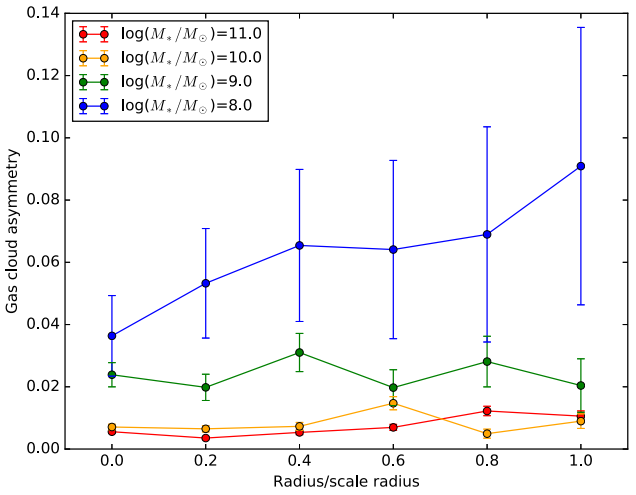

Figure 19. Radius (normalized over scale radius) against gas cloud asymmetry for each of the four simple model galaxies. The gas cloud asymmetry is inversely proportional to stellar mass at all radii. Uncertainties are binomial 1σ errors calculated following Cameron (2011).

(Bland-Hawthorn et al. 2010). There is some indication that cloud mass may scale with velocity dispersion and stellar mass surface density, as in Krumholz & McKee (2005), but this trend is likely to be comparatively weak.

(ii) that the H I gas fraction decreases monotonically with stellar mass. This assumption is broad, but serves to illustrate the general trend. We fit a line to the gas fractions estimated for our sample in equation (11) and our stellar masses to determine the gas fraction for each of our model galaxies.

(iii) that the presence of gas clouds relates directly to star formation, one for one, through the Schmidt–Kennicutt law. In reality, there might be rich gaseous regions of the galaxy that have no star formation at a given phase in its evolution. The relation between star formation rate and gas surface density further depends on properties of the turbulence, in particular the Mach number (Federrath 2013; Salim, Federrath & Kewley 2015).

(iv) that all gas is in the form of clouds. This may not be a realistic assumption, but it is reasonable to assume that clouds will form at proportionately the same rate in high- and low-mass galaxies [supported by the cloud counts in Bolatto et al. (2008)], so changing the fraction of gas mass that is formed into clouds will not affect the relative results for galaxies of different masses.

We calculate the asymmetry in distribution of gas clouds by taking the maximal difference between counts of gas clouds in quadrants, normalized over the total number of gas clouds in the radial bin:

$$\text{Gas cloud asymmetry} = \frac{|N_{\text{clouds,A}} - N_{\text{clouds,B}}|}{N_{\text{clouds,tot}}}_{\text{max}} \quad (13)$$

where $N_{\text{clouds, A}}$ and $N_{\text{clouds, B}}$ are cloud counts in different quadrants and $N_{\text{clouds, tot}}$ is the total cloud count in the radial bin.

Fig. 19 shows gas cloud asymmetry values for each of the six radial bins in each model galaxy, calculated for 1000 iterations of the random number generator. We observe a pronounced trend in which low-mass galaxies have a more numerically asymmetric distribution of gas clouds, at all radii, than high-mass galaxies.

Whilst this is a preliminary model, and does not incorporate many of the complexities which may affect gas cloud distribution, it illustrates the fundamental point that decreased gas mass leads to asymmetries in cloud distribution. This tendency towards 'clumpy' star-forming regions may lead to the trends for low-mass galaxies observed in the SAMI Galaxy Survey sample. Ashley, Simpson & Elmegreen (2013) show that morphological and kinematic asymmetry in low-mass, low-redshift galaxies is linked. They identify two galaxies from the Local Irregulars That Trace Luminosity Extremes in The H I Nearby Galaxy Survey (LITTLE THINGS) sample which have clumpy, asymmetrically distributed H I clouds and highly disturbed H I kinematics in corresponding regions. They proceed from the assumption that asymmetry is caused by interaction, and are thus surprised by the isolation of some disturbed, low-mass galaxies in the LITTLE THINGS sample. Here, we speculate that the distribution of gas clouds in low-gas-mass galaxies provides a mechanism by which low-mass galaxies may become perturbed in the absence of either ongoing or recent interactions. Johnson et al. (2012) also connect asymmetric clouds of H I gas with irregular H I rotation, and thence to disturbed Hα morphology.

Moiseev & Lozinskaya (2012) connect the magnitude of turbulent motion in dwarf galaxies to regions of high star formation, corresponding to gas clouds. They link local Hα surface brightness to regions of high dispersion, such that maximum velocity dispersion is seen in areas of low Hα surface brightness. That is, regions of high velocity dispersion are associated with areas surrounding regions of active star formation. Moiseev, Tikhonov & Klypin (2015) further argue that the velocity of turbulence in ionized gas is determined by star formation. Given that star formation is expected to be concentrated in giant molecular gas clouds (Blitz et al. 2007), it is plausible that the asymmetry of gas cloud distribution in Fig. 19 may lead to star formation in low-mass galaxies being unevenly distributed over the disc. In low-mass galaxies, the turbulence associated with star-forming regions as in Moiseev & Lozinskaya (2012) and Moiseev et al. (2015) may be larger, relative to the underlying disc rotation, than in high-mass galaxies.

The results and discussion presented here suggest several interesting directions for future work. Higher resolution kinematic maps, combined with imaging, of a statistical sample of local dwarf galaxies would enable the resolution of individual gas clouds and regions of star formation in both the kinematic and morphological regimes. Simulations with greater spatial resolution than SAMI may be able to provide the necessary data. We would then be able to trace the correspondence between asymmetric gas cloud distribution and kinematic disturbance more directly.

Deep imaging would also provide a more reliable merger indicator than the M_{20}/Gini plane. Whilst the M_{20}/Gini plane may be used to identify a sample of galaxies which are most likely mergers; it is not clear that all mergers in the sample are identified. This would provide an important standard against which to calibrate $\overline{v_{\text{asym}}}$ values.

Finally, it is possible that there is a relationship between star formation and $\overline{v_{\text{asym}}}$. Bloom et al. (2017b) found that there was no increase in global star formation for galaxies with $\overline{v_{\text{asym}}} > 0.065$, but that there was a small increase in concentration of star formation. Further investigation of the links between concentration and the cloud geometry described here would be useful in determining whether star formation is causally linked to asymmetry.

6 CONCLUSIONS

Whilst distance to first nearest neighbour, d_1, and thus interaction, plays some role in determining $\overline{v_{\text{asym}}}$, stellar mass is by far the strongest influence on kinematic asymmetry. Differences in relationships between d_1 and $\overline{v_{\text{asym}}}$, $\frac{\sigma_{\text{m}}}{V}$ and PA offset for high and low

stellar mass galaxies point to qualitative differences between the samples.

We find no relationship between distance to fifth nearest neighbour and $\overline{v_{\rm asym}}$.

For galaxies with $\log(M_*/{\rm M}_\odot) > 10.0$, there is an inverse relationship between d_1 and $\overline{v_{\rm asym}}$, pointing to interactions as a source of kinematic asymmetry for high-mass galaxies. Placement above the fiducial line on the M_{20}/Gini plane supports this.

However, for galaxies with $\log(M_*/{\rm M}_\odot) < 10.0$, a sample which includes many of the most asymmetric galaxies in our data set, there is no such relationship. We thus surmise that, for low stellar mass galaxies, there is a separate source of asymmetry beyond interaction.

Low stellar mass galaxies have higher $\frac{\sigma_{\rm m}}{V}$ than high-mass galaxies. We also define a parameter T, representing asymmetry as a fraction of dispersion, and find that low stellar mass galaxies are more dispersion-supported for given values of asymmetry.

We propose two potential causes of increased turbulence in low stellar mass galaxies: increased gas fraction and decreased total gas mass. After preliminary investigation, gas mass appears to be the dominant influence, although further investigation of these effects will be the subject of future work. We suggest that higher resolution kinematic maps and deep imaging will be helpful in the future, in order to better trace the link between gas clouds and asymmetric gas kinematics.

ACKNOWLEDGEMENTS

The SAMI Galaxy Survey is based on observations made at the Anglo-Australian Telescope. The Sydney-AAO Multi-object Integral field spectrograph (SAMI) was developed jointly by the University of Sydney and the Australian Astronomical Observatory. The SAMI input catalogue is based on data taken from the SDSS, the GAMA Survey and the VST ATLAS Survey. The SAMI Galaxy Survey is funded by the Australian Research Council Centre of Excellence for All-sky Astrophysics (CAASTRO), through project number CE110001020, and other participating institutions. The SAMI Galaxy Survey website is http://sami-survey.org/.

GAMA is a joint European–Australasian project based around a spectroscopic campaign using the Anglo-Australian Telescope. The GAMA input catalogue is based on data taken from the SDSS and the UKIRT Infrared Deep Sky Survey. Complementary imaging of the GAMA regions is being obtained by a number of independent survey programmes including *GALEX* MIS, VST KiDS, VISTA VIKING, WISE, *Herschel*-ATLAS, GMRT ASKAP providing UV to radio coverage. GAMA is funded by the STFC (UK), the ARC (Australia), the AAO, and the participating institutions. The GAMA website is http://www.gama-survey.org/.

Support for AMM is provided by NASA through Hubble Fellowship grant HST-HF2-51377 awarded by the Space Telescope Science Institute, which is operated by the Association of Universities for Research in Astronomy, Inc., for NASA, under contract NAS5-26555.

SMC acknowledges the support of an Australian Research Council Future Fellowship (FT100100457).

MSO acknowledges the funding support from the Australian Research Council through a Future Fellowship (FT140100255).

We thank Á. R. López-Sánchez for assisting in the proofreading of the paper.

REFERENCES

Abraham R. G., Van Den Bergh S., Nair P., 2003, ApJ, 588, 218
Ahn C. P. et al., 2014, ApJS, 211, 17
Amorín R., Vílchez J. M., Hägele G., Firpo V., Pérez-Montero E., Papaderos P., 2012, ApJ, 754, L22
Ashley T., Simpson C. E., Elmegreen B. G., 2013, AJ, 146, 42
Barrera-Ballesteros J. et al., 2015, A&A, 579, A45
Barton E. J., Geller M. J., Bromley B. C., van Zee L., Kenyon S. J., 2001, AJ, 121, 625
Bland-Hawthorn J., Krumholz M. R., Freeman K., 2010, ApJ, 713, 166
Bland-Hawthorn J. et al., 2011, Opt. Exp., 19, 2649
Blitz L., Fukui Y., Kawamura A., Leroy A., Mizuno N., Rosolowsky E., 2007, Protostars and Planets V, University of Arizona Press, Tucson, p. 81
Bloom J. et al., 2017a, MNRAS, 472, 1809
Bloom J. V. et al., 2017b, MNRAS, 465, 123
Bolatto A. D., Leroy A. K., Rosolowsky E., Walter F., Blitz L., 2008, ApJ, 686, 948
Brough S. et al., 2013, MNRAS, 435, 2903
Bryant J., O'Byrne J., Bland-Hawthorn J., Leon-Saval S., 2011, MNRAS, 415, 2173
Bryant J., Bland-Hawthorn J., Fogarty L., Lawrence J., Croom S., 2014, MNRAS, 438, 869
Bryant J. et al., 2015, MNRAS, 447, 2857
Byrd G., Valtonen M., 1990, ApJ, 350, 89
Cameron E., 2011, Publ. Astron. Soc. Aust., 28, 128
Cannon J. M., McClure-Griffiths N. M., Skillman E. D., Côté S., 2004, ApJ, 607, 274
Cappellari M., 2002, MNRAS, 333, 400
Cappellari M. et al., 2011, MNRAS, 413, 813
Casteels K. R. et al., 2013, MNRAS, 429, 1051
Cecil G. et al., 2016, MNRAS, 456, 1299
Cole S., Helly J., Frenk C. S., Parkinson H., 2008, MNRAS, 383, 546
Conselice C. J., Chapman S. C., Windhorst R. A., 2003, ApJ, 596, L5
Conselice C. J., Rajgor S., Myers R., 2008, MNRAS, 386, 909
Cortese L., Catinella B., Boissier S., Boselli A., Heinis S., 2011, MNRAS, 415, 1797
Croom S. M. et al., 2012, MNRAS, 421, 872
Darg D. et al., 2010, MNRAS, 401, 1043
Driver S. P. et al., 2009, Astron. Geophys, 50, 5
Driver S. P. et al., 2011, MNRAS, 413, 971
Ellison S. L., Mendel J. T., Patton D. R., Scudder J. M., 2013, MNRAS, 435, 3627
Emsellem E., Monnet G., Bacon R., 1994, A&A, 285, 723
Escala A., Larson R. B., 2008, ApJ, 685, L31
Federrath C., 2013, MNRAS, 436, 3167
Federrath C. et al., 2017, MNRAS, 468, 3965
Garrido O., Marcelin M., Amram P., Balkowski C., Gach J., Boulesteix J., 2005, MNRAS, 362, 127
Geha M., Blanton M., Masjedi M., West A., 2006, ApJ, 653, 240
Gini C., 1912, Pizetti E, Salvemini T, eds. Reprinted in Memorie di metodologica statistica. Libreria Eredi Virgilio Veschi, Rome p. 1
Glasser G. J., 1962, J. Am. Stat. Assoc., 57, 648
Green A. W. et al., 2014, MNRAS, 437, 1070
Ho I.-T. et al., 2016, MNRAS, 457, 1257
Hopkins P. F. et al., 2010, ApJ, 724, 915
Huang S., Haynes M. P., Giovanelli R., Brinchmann J., Stierwalt S., Neff S. G., 2012, AJ, 143, 133
Johnson M., Hunter D. A., Oh S.-H., Zhang H.-X., Elmegreen B., Brinks E., Tollerud E., Herrmann K., 2012, AJ, 144, 152
Kelvin L. S. et al., 2012, MNRAS, 421, 1007

Krajnović D., Cappellari M., De Zeeuw P. T., Copin Y., 2006, MNRAS, 366, 787
Krajnović D. et al., 2011, MNRAS, 414, 2923
Krumholz M. R., McKee C. F., 2005, ApJ, 630, 250
Lelli F., Verheijen M., Fraternali F., 2014, A&A, 566, A71
Lotz J. M., Primack J., Madau P., 2004, AJ, 128, 163
Lotz J. M., Jonsson P., Cox T., Croton D., Primack J. R., Somerville R. S., Stewart K., 2011, ApJ, 742, 103
Mahajan S. et al., 2015, MNRAS, 446, 2967
Moiseev A. V., Lozinskaya T. A., 2012, MNRAS, 423, 1831
Moiseev A. V., Tikhonov A. V., Klypin A., 2015, MNRAS, 449, 3568
Neistein E., Dekel A., 2008, MNRAS, 388, 1792
Owers M. et al., 2017, MNRAS, 468, 1824
Peebles P., 1982, ApJ, 263, L1
Roberts M. S., Haynes M. P., 1994, ARA&A, 32, 115
Robotham A. S. et al., 2011, MNRAS, 416, 2640
Robotham A. et al., 2014, MNRAS, 444, 3986
Salim D. M., Federrath C., Kewley L. J., 2015, ApJ, 806, L36
Shapiro K. L. et al., 2008, ApJ, 682, 231
Sharp R. et al., 2006, Proc. SPIE, 6269, 62690G
Sharp R. et al., 2015, MNRAS, 446, 1551
Taylor E. N. et al., 2011, MNRAS, 418, 1587
van Zee L., Skillman E. D., Salzer J. J., 1998, AJ, 116, 1186
Wisnioski E. et al., 2011, MNRAS, 417, 2601

APPENDIX A: CORRELATION COEFFICIENTS FOR VARIABLE MASS RANGES

Fig. A1 shows Spearman rank correlation parameters ρ and p for the relationship between $\log(M_*/\mathrm{M}_\odot)$ and $\overline{v_{\mathrm{asym}}}$ for samples with variable ranges of stellar mass. The largest stellar mass range for which there is a (small) statistically significant Spearman rank correlation is $9.05 < \log(M_*/\mathrm{M}_\odot) < 11.5$, with $\rho = -0.08$, $p = 0.05$. The correlation increases in strength and decreases in p with increasing minimum stellar mass. The smallest cutoff we consider is $10.5 < \log(M_*/\mathrm{M}_\odot) < 11.5$ because there are not enough galaxies at high stellar mass for higher cutoffs.

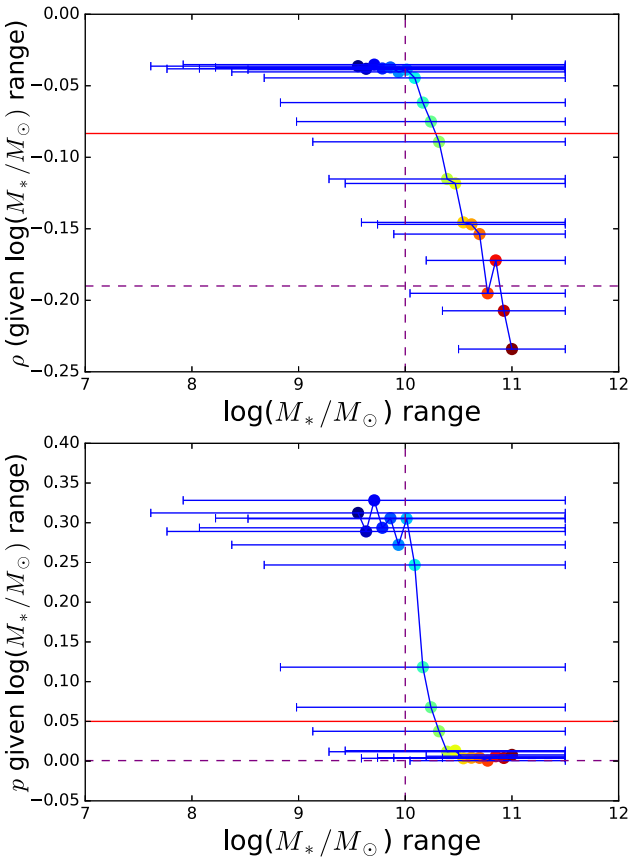

Figure A1. Spearman rank correlation parameters ρ and p for the relationship between $\log(M_*/\mathrm{M}_\odot)$ and $\overline{v_{\mathrm{asym}}}$ for samples with variable stellar mass ranges, indicated by the error bars. For example, the purple dashed lines show the ρ and p for galaxies with $10 < \log(M_*/\mathrm{M}_\odot) < 11.5$ ($\rho = -0.19$, $p = 7 \times 10^{-4}$). The red line indicates $p = 0.05$ (and corresponding ρ on the left panel). That is, there is a (small) statistically significant Spearman rank correlation for $9.05 < \log(M_*/\mathrm{M}_\odot) < 11.5$, with $\rho = -0.08$, $p = 0.05$. The correlation increases in strength and decreases in p with increasing minimum stellar mass.

This paper has been typeset from a TEX/LATEX file prepared by the author.